NeuroImage 54 (2011) 264–277

Contents lists available at ScienceDirect

NeuroImage

journal homepage: www.elsevier.com/locate/ynimg

Imaging dopamine receptors in humans with [^{11}C]-(+)-PHNO: Dissection of D3 signal and anatomy

Andri C. Tziortzi [a,b], Graham E. Searle [a], Sofia Tzimopoulou [a], Cristian Salinas [a], John D. Beaver [a], Mark Jenkinson [b], Marc Laruelle [a,d], Eugenii A. Rabiner [a,d], Roger N. Gunn [a,c,d,*]

[a] GlaxoSmithKline, Clinical Imaging Centre, Imperial College, London, UK
[b] FMRIB centre, Department of Clinical Neurology, University of Oxford, Oxford UK
[c] Department of Engineering Science, University of Oxford, Oxford, UK
[d] Division of Neuroscience and Mental Health, Imperial College, London, UK

ARTICLE INFO

Article history:
Received 16 February 2010
Revised 12 May 2010
Accepted 16 June 2010
Available online 30 June 2010

Keywords:
dopamine D3 receptors
PET
PHNO
region of interest
ROI
ventral striatum
VST
ventral pallidum
hypothalamus
extended amygdala

ABSTRACT

[^{11}C]-(+)-PHNO is a D3 preferring PET radioligand which has recently opened the possibility of imaging D3 receptors in the human brain *in vivo*. This imaging tool allows characterisation of the distribution of D3 receptors *in vivo* and further investigation of their functional role. The specific [^{11}C]-(+)-PHNO signal is a mixture of D3 and D2 components with the relative magnitude of each component determined by the regional receptor densities. An accurate and reproducible delineation of regions of interest (ROI) is therefore important for optimal analysis of human PET data. We present a set of anatomical guidelines for the delineation of D3 relevant ROIs including substantia nigra, hypothalamus, ventral pallidum/substantia innominata, ventral striatum, globus pallidus and thalamus. Delineation of these structures using this approach allowed for high intra- and inter-operator reproducibility. Subsequently we used a selective D3 antagonist to dissect the total [^{11}C]-(+)-PHNO signal in each region into its D3 and D2 components and estimated the regional fraction of the D3 signal (f^{D3}_{PHNO}). In descending order of magnitude the following results for the f^{D3}_{PHNO} were obtained: hypothalamus = 100%, substantia nigra = 100%, ventral pallidum/substantia innominata = 75%, globus pallidus = 65%, thalamus = 43%, ventral striatum = 26% and precommissural-ventral putamen = 6%. An automated approach for the delineation of these anatomical regions of interest was also developed and investigated in terms of its reproducibility and accuracy.

Introduction

Since its discovery, dopamine has been implicated in the control of movement and cognition and has also emerged as a key factor in diverse brain diseases such as Parkinson's disease, schizophrenia and drug addiction (Cumming, 2009). Dopaminergic neurotransmission is transducted via five G-protein-coupled receptors (GPCRs), dopamine-D_1 (D_1R) to dopamine-D_5 (D_5R). The dopamine receptors (DRs) constitute two families, the D_1-like (D_1R and D_5R) and the D_2-like (D_2R, D_3R and D_4R) family. The D_2-like family of receptors are coupled to G_i/G_o G-proteins (as opposed to the G_s coupling of the D_1-like family), and the density of expression of D_2R is significantly higher than that of D_3R and D_4R. The D_3R were first characterised in 1990 by Sokoloff et al. (1990). Their distribution in brain areas linked with functional aspects of motivation and reward made them an attractive target for the treatment of addictive disorders.

Studies exploring the distribution of the D_3 receptors in the human brain using post-mortem tissue (Murray et al., 1994; Staley and Mash, 1996; Gurevich and Joyce, 1999) report a declining rostral to caudal gradient of D_3R in the striatum as well as the existence of D_3R in some extra-striatal locations, such as the substantia nigra (SN), and thalamus (TH). In the striatum, the D_3R are particularly enriched in the nucleus accumbens (NAC) and the precommissural ventral putamen (preVPU). The presence of D_3R sites and mRNA was demonstrated in the pallidum (Murray et al., 1994; Gurevich and Joyce, 1999) with the highest concentrations found in the internal segment of the globus pallidus (GP) and the ventral pallidum (VP). Gurevich and Joyce (1999) and Staley and Mash (1996) also documented the existence of D_3 receptors in the anterior ventral thalamus and throughout the hypothalamus (Hypo) though at considerably lower levels than in the striatum and pallidum. Gurevich stressed the relative abundance of the D_3 sites in the mammilothalamic tract (MMT) and the mammilary bodies (MB) of hypothalamus.

Despite these in-vitro findings, the in-vivo examination of D_3R has been limited due to the lack of a selective PET ligand. The introduction of [^{11}C]-(+)-PHNO (Wilson et al., 2005) has opened the possibility of imaging the D_3R. [^{11}C]-(+)-PHNO was initially introduced as a potent

* Corresponding author. GlaxoSmithKline, Clinical Imaging Centre, Imperial College London, Hammersmith Hospital, Du Cane Road, London W12 0NN, UK. Fax: +44 208 008 6491.
E-mail address: roger.n.gunn@gsk.com (R.N. Gunn).

1053-8119/$ – see front matter © 2010 Elsevier Inc. All rights reserved.
doi:10.1016/j.neuroimage.2010.06.044

agonist radioligand suitable for imaging the high affinity state of the D_2R (D_2^{high}) (Willeit et al., 2006). At the same time, Narendran and colleagues (2006) demonstrated that [^{11}C]-(+)-PHNO is a D_3 preferring radioligand, using the D_3 preferring blocker BP-897 in non-human primates. Further characterisation of the binding of [^{11}C]-(+)-PHNO *in vivo* in non-human primates and D_2R and D_3R knock-out mice confirmed the preferential selectivity of [^{11}C]-(+)-PHNO for D_3R over D_2R, and characterised the D_2R and D_3R components of [^{11}C]-(+)-PHNO binding in different brain areas (Rabiner et al., 2009). A formal investigation of the relative D_2R and D_3R affinities of [^{11}C]-(+)-PHNO *in vivo* in the primate brain found a ~20-fold selectivity for D_3R over D_2R (Gallezot et al., 2009). In humans, using selective D_3R antagonists, the [^{11}C]-(+)-PHNO binding profile has been shown to be consistent with that found in non-human primates. (Searle et al., 2010).

The [^{11}C]-(+)-PHNO binding is a mixture of D_3 and D_2 components whose relative contribution varies regionally. An accurate and reproducible delineation of regions of interest (ROIs) is therefore important for optimal analysis. The aim of this present study is to optimise the methodology for the analysis of human [^{11}C]-(+)-PHNO studies and to explore the D_3R distribution in the human brain *in vivo*. Firstly, we present a set of criteria for the anatomical delineation of D_3 relevant ROIs. Secondly, manual and automated approaches for the delineation of these ROIs are investigated in terms of their reproducibility and accuracy. Thirdly, the regional [^{11}C]-(+)-PHNO signal is dissected into its D_3 and D_2 components using a selective D_3 antagonist.

Materials and methods

Subjects

Nineteen healthy male volunteers, free from clinically significant illness or disease as determined by their medical history and standard laboratory tests, had [^{11}C]-(+)-PHNO PET and MRI scans. All PET scans were conducted at the Centre of Addiction and Mental Health in Toronto, Canada. Subjects were scanned at baseline and following the administration of a selective D_3 blocker (GSK598809) at doses of 5 mg to 175 mg. GSK598809 is a selective D_3R antagonist which exhibits a 500-fold selectivity for the D_3R over the D_2R in vitro (Searle et al., 2010) The data presented here are obtained from the cohort described previously by Searle et al. (2010).

PET data

In total, 48 PET scans were acquired on a Siemens Biograph HiRez XVI PET tomograph (Siemens Healthcare). Subjects were positioned in the scanner and movement was minimised by using a custom-made thermoplastic facemask together with a head-fixation system (Tru-Scan Imaging, Annapolis, Maryland). Subjects were injected with a single intravenous bolus of [^{11}C]-(+)-PHNO between 235 and 368 MBq (mean = 307.2, SD = 40.6) with specific activity ranging between 23.3 and 38.6 GBq/μmol (mean = 32.24, SD = 4.58) at the time of injection. The mass of injected [^{11}C]-(+)-PHNO was between 2 and 2.6 μg (mean = 2.36, SD = 0.13) and the radiochemical purity of the compound was 97.7–99.9% (mean = 99.4, SD = 0.6). Following bolus administration of [^{11}C]-(+)-PHNO, dynamic emission data were acquired for 90 minutes (1×30s, 8×15 s, 3×1 min, 5×2 min, 5×5 min, and 5×10 min). A low-dose CT scan (effective dose = 0.2 mSv) was also acquired and used for attenuation correction and model-based scatter correction. The dynamic images were reconstructed using Fourier rebinning and a 2D filtered back projection algorithm with a ramp filter at Nyquist cut off frequency (Defrise et al., 1997).

MRI data

T1-weighted and proton density (PD) MRI images were acquired on a GE Medical system Signa EXCITE HD, 1.5 T. The structural T1-weighted images (acquired in the axial plane: FSPGR-IR PREPPED, TR = 12.008, TE = 5.1160, flip angle = 20°, slice thickness = 0.78 × 0.78 × 1.5 mm) were acquired to aid in the definition of the subcortical ROIs. The PD images (FSE PD, TR = 6000, TE = 12.1920, flip angle = 90°, slice thickness = 0.86 × 0.86 × 3 mm) were acquired to help define the size and orientation of the SN ROI.

Image analysis

The MR and PET images of each subject underwent a series of spatial processing steps. The non-brain voxels from the MR images were removed using the FSL Brain Extraction Tool (Smith, 2002) and the extracted brain was rigidly registered to the nonlinear ICBM152 template (http://www2.bic.mni.mcgill.ca/) (MNI space) using SPM5 (Wellcome Trust Centre for Neuroimaging) to bring subjects into a similar orientation and facilitate manual ROI delineation. PET images were corrected for motion by realigning each frame to a reference frame, using mutual information as a cost function, and then these were registered to the T1-MRI.

Regional analysis was performed with both manual and automatically delineated ROIs (see below MAN I, MAN II and AUTO). For the manual ROI delineation, the MRI was made isotropic to the smallest voxel size of the original image (0.79 × 0.79 × 0.79 mm) in order to obtain the best possible visual quality. For the automated method, the nonlinear ICBM152 template was non-linearly warped with SPM5 (Wellcome Trust Centre for Neuroimaging) to the high-resolution T1-MRI of each individual. The deformation parameters derived were then applied to an anatomical atlas (detailed below) to bring this into the individual subject's space. Finally, the MRI image, the ROIs and the warped anatomical atlas were resampled to match the PET image resolution (2 × 2 × 2 mm).

Derivation of the parameters of interest—BP_{ND} and D3 contribution to the total [^{11}C]-(+)-PHNO specific signal (f_{PHNO}^{D3})

[^{11}C]-(+)-PHNO binding potential (BP_{ND}) estimates were obtained by three separate analysis approaches: (A1) ROIs were applied to the dynamic PET data to derive regional time activity curves (TACs) before applying the simplified reference tissue model (SRTM) (Lammertsma and Hume, 1996), with the cerebellum as a reference region, to derive regional BP_{ND} estimates. (A2) The basis function implementation of SRTM (Gunn et al., 1997) was applied to the dynamic PET data to derive parametric images of BP_{ND} (parameter bounds in terms of non-decay corrected data: $\theta_3^{min} = 0.0008\ s^{-1}$ and $\theta_3^{max} = 0.5\ s^{-1}$; cf. Gunn et al., 1997). ROIs were then applied to the BP_{ND} images to derive regional BP_{ND} estimates. (A3) The parametric BP_{ND} images generated in A2 were nonlinearly warped onto the ICBM152 template and then ROIs defined on this template were applied to derive regional BP_{ND} estimates.

Using a single site competition model for the binding of [^{11}C]-(+)-PHNO (Searle et al., 2010), the BP_{ND} obtained following administration of the selective D_3 antagonist, GSK598809, can be described by:

$$BP_{ND}^{GSK598809} = BP_{ND}^{Baseline}\left[\frac{f_{PHNO}^{D3}}{1+\frac{C_P^{GSK598809}}{EC_{50}^{D3}}} + \left(1-f_{PHNO}^{D3}\right)\right] \quad (1)$$

where $BP_{ND}^{Baseline}$ and $BP_{ND}^{GSK598809}$ are the BP_{ND} values at baseline and following dosing with GSK598809, respectively, $C_P^{GSK598809}$ is the plasma concentration of GSK598809 and EC_{50}^{D3} is the half saturation concentration of GSK598809. Regional f_{PHNO}^{D3}were obtained by fitting the competition model in Eq. (1) to the BP_{ND} values obtained from methods A1 and A2 under the assumption that EC_{50}^{D3} was constant across all regions. All regional f_{PHNO}^{D3} derived from regional and parametric analyses were obtained from manually delineated ROIs

only defined with the method MAN I (see below). f^{D3}_{PHNO} was also estimated at the voxel level by fitting the competition model (Eq. (1)) to the spatially normalised parametric images in A3 and constraining EC^{D3}_{50} to the value estimated on a regional basis (A2). Parametric images of the D_3R and D_2R components of the total [^{11}C]-(+)-PHNO BP_{ND} signal were then generated using the voxel-level f^{D3}_{PHNO} and Eqs. (3) and (4), respectively. In Eqs. (3) and (4), the BP^{PHNO}_{ND} is the average [^{11}C]-(+)-PHNO template image obtained with the A3 approach.

$$BP^{PHNO}_{ND} = BP^{D3}_{ND} + BP^{D2}_{ND} \quad (2)$$

$$BP^{D3}_{ND} = f^{D3}_{PHNO} BP^{PHNO}_{ND} \quad (3)$$

$$BP^{D2}_{ND} = \left(1 - f^{D3}_{PHNO}\right) BP^{PHNO}_{ND} \quad (4)$$

Delineation of D_3 anatomy

ROIs were defined both by manual delineation and automatically via non-linear deformation of an atlas. These ROIs were then applied either to the dynamic images or directly onto parametric images to estimate the regional parameters. The ROIs included in each of these methods are shown in Table 1.

Manual delineation of ROIs

Subcortical ROIs relevant to the examination of D_3R were identified from autoradiography studies (Murray et al., 1994; Staley and Mash, 1996; Gurevich and Joyce, 1999), [^{11}C]-(+)-PHNO PET studies (Narendran et al., 2006; Willeit et al., 2006; Rabiner et al., 2009; Searle et al., 2010) and localisation of the dopaminergic tracts. A set of guidelines for the definition of these D_3 relevant ROIs were developed to balance the need to accurately encompass the region of interest and to ensure the reproducibility of this analysis. The guidelines are specific for images in MNI space. The ROIs defined with the guidelines presented in this paper will be noted as MAN I, with the detailed guidelines description found at the end of the "Materials and methods" section.

All ROIs except SN were defined on the high-resolution MR image using Analyze™ (Mayo Clinic, 1986). SN is a small region and due to its size and location the registration between PET and MRI around this area is not optimal. It is therefore preferable to define the SN ROI on a PET integral image using a fixed ROI size. The criteria chosen for striatal subdivisions were based on findings from in vitro studies (Murray et al., 1994; Staley and Mash, 1996; Gurevich and Joyce, 1999) (i.e. declining rostral to caudal gradient of D_3R) and the distribution of the [^{11}C]-(+)-PHNO signal.

Fig. 1. shows the delineation of ROIs on the MRI and PET images for a number of characteristic slices.

To provide a benchmark for the MAN I reproducibility, striatal ROIs were compared with a method developed previously at Columbia University PET Centre (this method will be noted as MAN II) for D_2R imaging with [^{11}C]Raclopride (Mawlawi et al., 2001; Martinez et al., 2003).

Automated delineation of ROIs

The automated delineation of ROIs is achieved by non-linear deformation of an anatomical atlas into the space of each individual. The subcortical ROIs of the atlas were manually defined on the non-linear ICBM152 template according to the guidelines developed for MAN I. This allows for a direct comparison between manual and automated methods.

Anatomical atlas

The atlas consists of a total of 119 regions (Fig. 2). The cortical regions are a modification of the Harvard–Oxford atlas which consists of 48 probabilistic maps derived from 37 healthy subjects. Four cortical regions (i.e. precuneous cortex, angular gyrus, superior parietal lobule and occipital pole) from the original Harvard–Oxford atlas were redefined on the ICBM152 template. For the remaining cortical regions, a threshold was applied to the probability map of each structure to achieve the best possible fit to the ICBM152 template. Some of these cortical regions were combined to create larger anatomical regions; some were kept the same, while others were subdivided (to reflect functional organisation) using anatomical landmarks.

The subcortical regions were defined on the non-linear ICBM152 template following the same guidelines as for MAN I while for TH the thalamic connectivity atlas, (FMRIB, Oxford University; Johansen-Berg et al., 2005) was used. Finally, the cerebellum and the brain stem were manually defined combining information from the SUIT (Diedrichsen, 2006) and ICBM152 templates. The brain stem is subdivided into three areas, midbrain, pons and medulla. The cerebellum consists of three regions: (a) dorsal cerebellum; (b) ventro-lateral cerebellum; and (c) medial cerebellum. Medial cerebellum includes structures such as the vermis and uvula. The subdivision of cerebellum into the aforementioned areas is useful for the PET studies where cerebellum is used as reference region (for example exclusion of the dorsal part of cerebellum is recommended if there is a need to avoid spillover effects from neighbouring high signal in the occipital cortex). The regions

Table 1
Region abbreviation, ROI volume and ROIs included in each method. MAN I is the method developed and presented in this paper for the ROI delineation; MAN II is a method developed by the Columbia University PET Centre; Auto is the automated approach for the ROI delineation.

Region	Region abbreviation	ROI volume (cm^3)	MAN I	MAN II	AUTO
Ventral pallidum/substantia innominata	VP_{SI}	0.1 ± 0.05	√		
Globus pallidus	GP	0.8 ± 0.1	√		√
Ventral striatum	VST	1.0 ± 0.1	√	√	√
Precommissural ventral putamen	preVPU	1.1 ± 0.2	√		√
Precommissural putamen	prePU	1.7 ± 0.2	√	√	√
Putamen	PU	3.1 ± 0.3	√	√	√
Precommissural dorsal putamen	preDPU	0.6 ± 0.1	√		√
Postcommisural putamen	posPU	1.4 ± 0.2	√	√	√
Precommisural caudate	preCD	2.0 ± 0.2	√	√	√
Caudate	CD	2.3 ± 0.3	√	√	√
Postcommisural caudate	posCD	0.3 ± 0.1	√	√	√
Hypothalamus	Hypo	0.5 ± 0.03	√		
Substantia nigra	SN	0.3[a]	√		
Thalamus	TH	5.3 ± 0.4	√		

[a] Fixed ROI size.

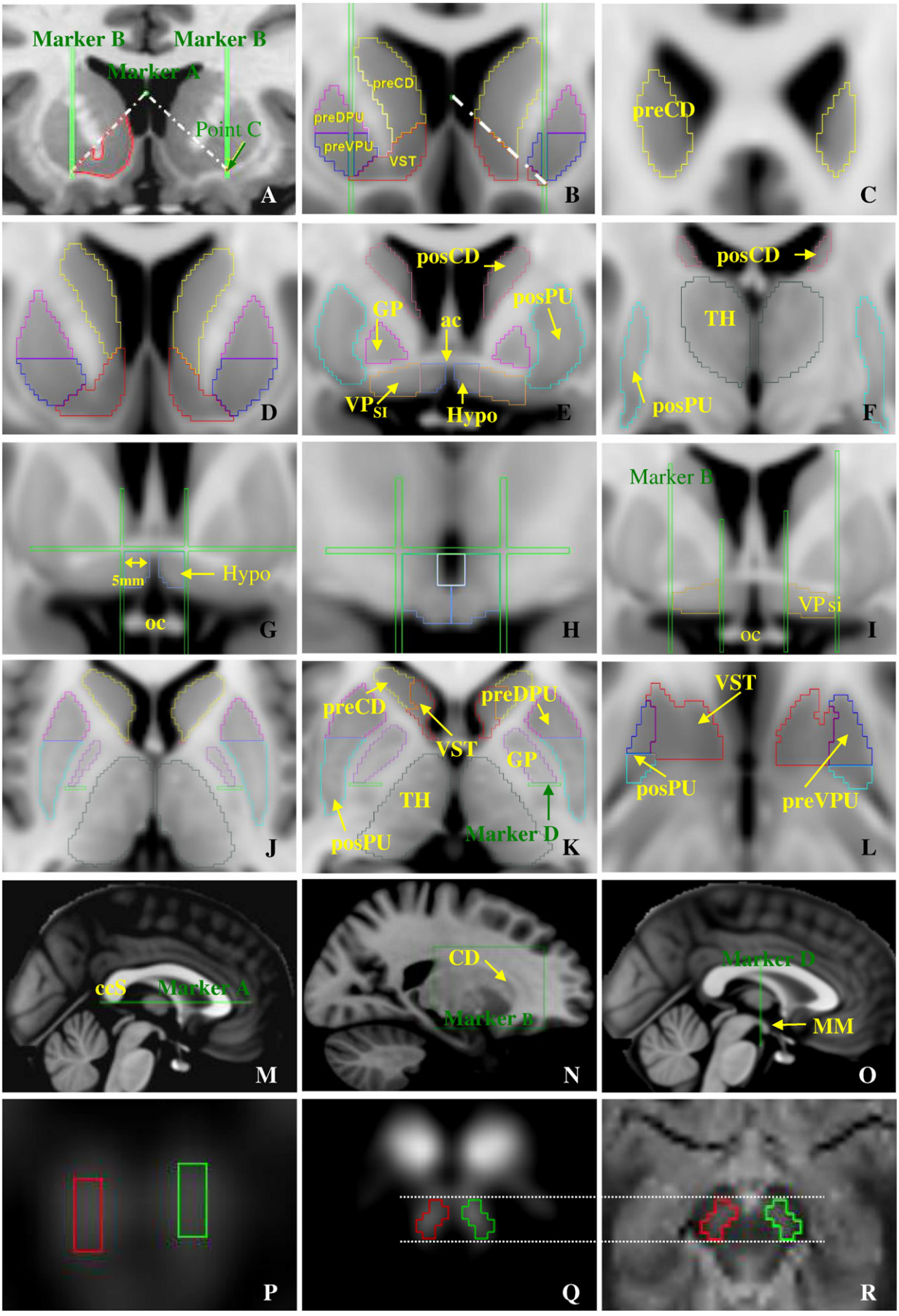

Fig. 1. Guidelines for the manual delineation of ROIs with method MAN I on T1_w MR (A–O) and PET (P-Q) images. R is a proton density (PD) image which was used to define the size of the SN ROI.

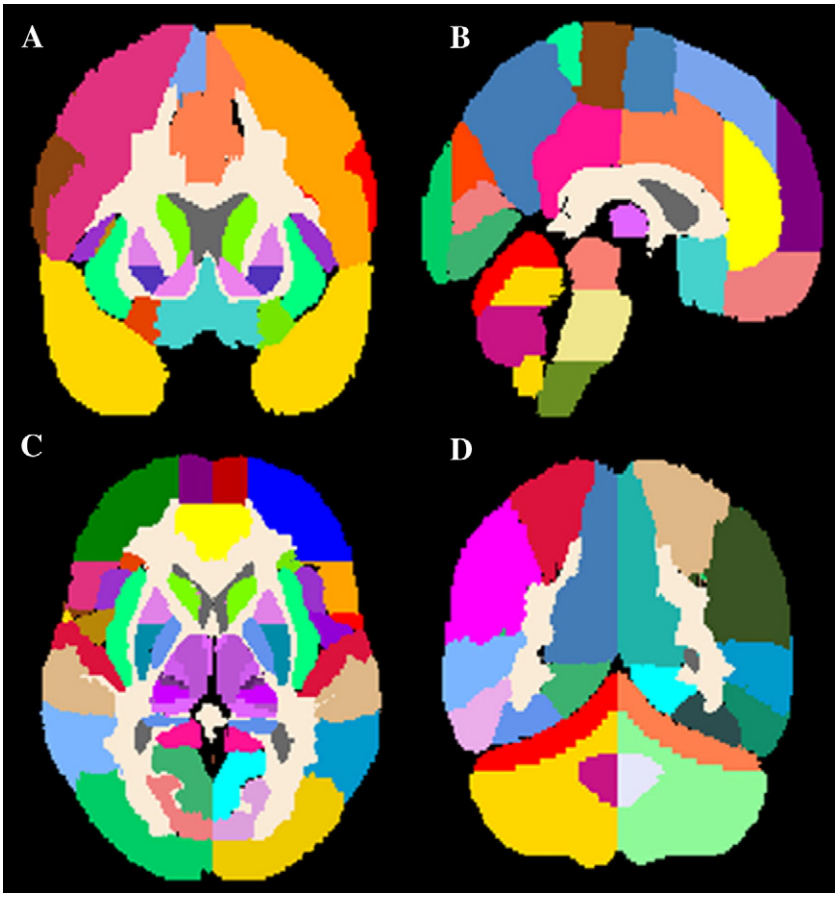

Fig. 2. Anatomical atlas. Cortical regions are a modification of the Harvard–Oxford atlas, subcortical ROIs were defined on the ICBM152 template following MAN I guidelines and thalamus was replaced by the thalamic connectivity atlas, obtained from FMRIB, Oxford University.

defined automatically using the anatomical atlas (Table 1) were compared with the ROIs defined manually with MAN I (Table 1).

Agreement and reproducibility metrics

The reproducibility of the manually defined ROIs and the level of agreement between the manual and automatically derived subcortical ROIs were examined.

The manually delineated ROIs are treated as the "gold-standard". However, manual delineation is subjective as it depends on the operator's knowledge of anatomy and interpretation of the guidelines. To examine the reproducibility of manual delineation, ROIs were delineated by two operators, twice each on two separate occasions (at least 1 month apart) according to the aforementioned guidelines. The same procedure was followed for both MAN I and MAN II, in order to provide a benchmark for the performance of MAN I in terms of reproducibility and the time taken to delineate the striatal structures.

The first metric calculated was the DICE coefficient which measures the degree of ROI volume overlap between two ROIs (Dice, 1945),

$$\mathrm{DICE} = 2 \cdot \frac{|\mathrm{ROI}_1 \cap \mathrm{ROI}_2|}{|\mathrm{ROI}_1 + \mathrm{ROI}_2|} \cdot 100\% \tag{5}$$

where ∩ is the intersection of the ROI volumes and ranges from 0 to 1. Thus, the DICE coefficient ranges from 0%, for ROIs with no overlap up to 100% for identical ROIs. The intra- and inter-operator ROI overlap was calculated for MAN I and MAN II. The second metric calculated was the variability of BP_{ND} (obtained with method A1) which is a measurement of reproducibility that depends both on the geometrical ROI overlap and the local dopamine receptor landscape,

$$\mathrm{Variability}\ BP_{ND} = 2 \cdot \left| \frac{\left(BP_{ND}^{ROI_1} - BP_{ND}^{ROI_2}\right)}{BP_{ND}^{ROI_1} + BP_{ND}^{ROI_2}} \right| \cdot 100\% \tag{6}$$

The intra-operator and inter-operator variability of BP_{ND} were calculated for MAN I and MAN II.

To measure the degree of agreement between MAN I and MAN II, the intra-class correlation coefficient (ICC) for the BP_{ND} values obtained with the two methods was calculated. The ICC was calculated as:

$$\mathrm{ICC} = \frac{\mathrm{BSMSS} - \mathrm{WSMSS}}{\mathrm{BSMSS} + \mathrm{WSMSS}} \tag{7}$$

where BSMSS is the mean sum of squares between subjects and WSMSS is the mean sum of squares within subjects.

The automated approach (AUTO) was compared with MAN I by calculating the inter–method DICE coefficient (subcortical regions only, excluding thalamus) and the inter-method variability of BP_{ND} using Eqs. (5) and (6), respectively.

ROI guidelines (MAN I)

The guidelines are developed for images in MNI space and are applicable only to images in this space. The following rules were applied during manual ROI delineation:

a. The outer limit of an anatomical structure as defined in anatomical books (Duvernoy, 1999) acts as the boundary for an ROI.

b. If reliable tracing of a portion of the boundary of an ROI could not be performed, this portion was excluded.

ROIs defined on the MRI image

Ventral striatum (VST)

Several studies have shown that there is not a definitive anatomical, histological or histochemical distinction between nucleus accumbens (NAC), CD and PU. Therefore, the dorsal boundary of VST was defined so as to include NAC, medial CD, rostroventral PU and also to be consistent with the functional anatomy of VST as defined in connectivity studies (Parent and Hazrati, 1995; Haber and McFarland, 1999; Haber et al., 2000; Cohen et al., 2009; Haber and Knutson, 2009). The dorsal boundary is defined by connecting two points (Marker A and Point C) on the coronal plane (Fig. 1A). These two points are predefined by the placement of two 3D markers (Markers A and B) on the sagittal plane (Figs. 1M and N). Marker A: a horizontal line intersecting the most ventral part of the splenium of the corpus callosum (ccS) is placed on the most midsagittal slice. Sometimes there are two or three slices which can be described as the "most midsagittal slice" and in this case the operator is advised to select the one where thalamus appears the smallest. In coronal view, Marker A appears as a single voxel in each slice (Fig. 1A, Marker A) and this voxel will be used for the definition of the dorsal boundary of VST. Marker B: Moving from lateral to medial on each hemisphere, a rectangle is placed on the first slice where the grey matter of the head of CD can be clearly seen. In a coronal view, this will appear as a voxel width column. The inferior intersection of this column with grey matter of PU, within this column, is defined as the point C (Figs. 1A and B). VST tracing begins when point C comes into view, up to the slice where anterior commissure connects the two hemispheres. However, there are occasions that the thin white matter layer which separates the VST area from subcallosal gyrus and/or septal nuclei cannot be observed, making it infeasible to sample the VST up to the anterior commissure (AC). Any white matter (e.g. internal capsule) should be excluded from the ROI (Fig. 1B, right VST). Figs. 1A, B and D show the VST delineation on three representative rostral to caudal slices. This is an optimisation of the previous VST definition, developed by the group at Columbia University (Mawlawi et al., 2001; Martinez et al., 2003), and aims to:

(i) more accurately encompass the VST as defined from functional studies (Parent and Hazrati, 1995; Haber and McFarland, 1999; Haber et al., 2000; Cohen et al., 2009);
(ii) increase reproducibility; and
(iii) reduce the time taken for delineation.

Caudate (CD)

Caudate is drawn wherever visible on the coronal plane. When the VST is present it is CD's inferior border. Care should be taken not to include cerebrospinal fluid from the ventricles (Figs. 1B–F). The anterior commissure subdivides the caudate into precommissural (preCD) and postcommissural (posCD).

Putamen (PU)

Putamen is defined on the transverse plane and it is traced on all slices where dense grey matter can be clearly observed and differentiated from surrounding structures (Figs. 1J–L). On the most ventral slices where the anterior commissure (AC) divides the PU into two regions the ROI includes only the grey matter that is anterior to the AC. PU is traced as a single ROI and subsequently it is subdivided into preDPU, preVPU and posPU by providing the position of the AC and posterior commissure (PC). The AC subdivides the PU into precomissural and postcomissural while the PC subdivides the precomissural PU into dorsal and ventral (Figs. 1B, D–E, J–L).

Globus Pallidus (GP)

Globus pallidus takes its name from the pale-appearance, which makes its delineation difficult and susceptible to misclassification since it is hard to discern from its surroundings. The GP ROI consists of both the external and internal GP since the subdivision was not feasible on this MR sequence. GP delineation is performed on the transverse plane, dorsal to ventral (Figs. 1J–K), and it is defined up to the slice where AC connects the two hemispheres. To increase the reproducibility of the tracing and exclude areas which might be misclassified (such as the corticospinal tract), a 3D marker (Marker D) is placed on the most midsagittal slice. This is a vertical line intersecting the posterior surface of the mamillarly body (MM) which becomes its posterior boundary on the transverse plane (Fig. 1O).

Thalamus (TH)

Thalamus is drawn on all of the transverse slices that it is visible–and drawing ends just before the superior colliculi becomes visible (Figs. 1J–K). The dorsal boundary changes between lateral ventricle and a thin layer of white matter. Internal capsule and third ventricle are the lateral and medial boundaries, respectively. The inferior boundary is either the CSF of the ventricles or the white matter of the fornix. The ROI should contain the full grey matter area so as to include the entire thalamic nuclei.

Hypothalamus (Hypo)

The hypothalamus is traced on the coronal plane and tracing starts from the first slice where the AC connects the two hemispheres up to the slice where the Mammilary bodies (MB) are joined. Marker D (Fig. 1O) can be used as the caudal boundary of this delineation. A dorsal and a bilateral boundary are defined to enable the tracing of the region (Figs. 1G–H). The dorsal boundary is a horizontal line that intersects the inferior part of the AC and it is copied on all slices of interest. The lateral boundary is defined on a sagittal slice 5 mm bilateral from the first medial slice where the hypothalamus can be observed.

Ventral pallidum/substantia innominata (VPSI)

Ventral pallidum is not easy to define in humans as there is an admixture of the ventral pallidum and ventral striatum in the area under the anterior commissure. For this reason, the proposed guidelines are referring to a ventral Pallidum/ substantia innominata ROI (VP_{SI}). The VP_{SI} is defined on the coronal plane (Figs. 1E and I). The tracing starts at the slice where AC connects the two hemispheres and stops at the slice where AC does not separate GP from VP_{SI} (~3 slices on a $1\times1\times1$ mm MRI). The medial boundary is a vertical line intersecting the medial edge of the optic chiasm (OC) and it is placed on the first slice that the AC interconnects the two hemispheres as viewed on a coronal plane and copied on to the subsequent slices of interest. Marker B (see VST definition and Fig. 1N) is the lateral boundary. The superior boundary is the white matter of AC and the inferior boundary is the CSF or white matter. VP_{SI} is the grey matter that can be sampled within these boundaries. However, due to the complicated anatomy of this area, the ROI might include regions such as anterior perforated substance or septal nuclei. There are cases when this region cannot be clearly defined due to signal drop out and partial volume effects. Care should be taken in order to exclude PU, GP and CD grey matter.

ROIs defined on the PET

Substantia nigra

SN is located in the midbrain and is a small region with no clear cut boundaries. Due to its small size and potential mis-registration issues between the PET and MRI images, the SN ROI is defined on the PET integral image. However, the size of a given anatomical structure as

Table 2
ROI size of substantia nigra. These ROIs are placed on a 2×2×2 mm PET image. The magnitudes are in the following order: Width×Height in mm, Angle in degrees. The first slice corresponds to the most ventral ROI placement while the fifth to the most dorsal ROI placement.

Number of slices, ventral to dorsal	Right hemisphere	Left hemisphere
1st slice	4×8 mm, 0°	4×8 mm, 0°
2nd slice	4×10 mm, 0°	4×10 mm, 0°
3rd slice	6×12 mm, 25°	6×12 mm, 25°
4th slice	6×12 mm, 25°	6×12 mm, −25°
5th slice	4×10 mm, 25°	4×10 mm, −25°

determined from a PET image could be affected by the minimum and maximum intensity values as well as by the physiological and pharmacological conditions of the experiment. Fixed size ROIs (right and left) are used in order to minimise variability induced by these factors. The ROIs are placed on five successive transverse slices (2 mm thickness) vertically centred on the maximal PET signal in SN. The sizes of the ROIs are given in Table 2. In each of the five selected transverse slices, a rectangle of the specified size is placed over each of the two hotspots, with default rotation as specified in Table 2, though modifications to the angle are permitted if this results in improved alignment. The size of the ROIs and the proposed angles are based on information acquired from the PD-weighted MRI images of each subject where the SN can be clearly seen (Figs. 1R).

Results

All 48 [^{11}C]-(+)-PHNO PET scans and corresponding MR scans from the 19 subjects were analysed successfully to derive regional and parametric estimates of BP_{ND} and f^{D3}_{PHNO}. A good description of the kinetic data was achieved using SRTM. Fig. 3 shows regional model fits for a representative subject at baseline and post-GSK598809 for SN, Hypo, VST, ventral pallidum/substantia innominata (VP_{SI}), GP, TH and cerebellum. The radioactive counts in all regions peaked early but have different wash out rates depending on the relative contribution of dopamine D_3 and D_2 receptors. A representative distribution of [^{11}C]-(+)-PHNO BP_{ND} in one subject at baseline and after administration of the selective D_3 antagonist (GSK598809) compound is shown in Fig. 4. A high accumulation of [^{11}C]-(+)-PHNO is observed in the striatum, pallidum (GP and VP_{SI}), Hypo amd SN and a lower heterogeneous signal in the TH. After the administration of GSK598809, a substantial BP_{ND} reduction is observed in the pallidum, Hypo and SN.

Agreement and reproducibility of manual and automated ROIs

We have presented guidelines for the definition of the D_3 regions of interest (MAN I) including Hypo, SN, Striatum, GP, VP_{SI} and TH. To delineate the whole set of ROIs for one subject using MAN I takes approximately 5 hours for an experienced operator with striatum and GP being the most demanding ROIs in terms of complexity and time taken. The reproducibility of the manual ROIs was assessed in terms of ROI volume overlap (DICE) and BP_{ND} variability. The average intra-operator DICE across ROIs for MAN I was 88 ± 6% with the lowest DICE value obtained in VP_{SI} and the highest value in TH (Fig. 5). To provide a benchmark of reproducibility for MAN I, striatal ROIs were defined with method MAN II. MAN I requires between 2 and 3 hours to delineate the striatum while MAN II takes between 2.5 and 3.5 hours. The intra-operator DICE for MAN I and MAN II, respectively, were 88 ± 2% over 78 ± 3% for VST, 90 ± 1% over 87 ± 1% for PU and 91 ± 1% over 88 ± 1% for CD (Fig. 5). The average inter-operator DICE for MAN I was 81 ± 10% with the lowest DICE obtained for VP_{SI} and the highest for TH (Fig. 5). In striatum the inter-operator DICE values for MAN I and MAN II were 79 ± 3% and 74 ± 4% for VST, 87 ± 2% and 84 ± 2% for PU and 84 ± 2% and 84 ± 2% for CD (Fig. 5). As with the intra-operator DICE, the inter-operator DICE for MAN I was higher than for MAN II, but overall both methods provide highly reproducible results. The DICE coefficients for all regions are shown in Fig. 5. To assess the similarity between MAN I and MAN II, we estimated the volume overlap between the ROIs defined with the two methods (VST DICE = 66 ± 4%, CD DICE = 87 ± 1% and PU DICE = 81 ± 1%).

The average intra-operator BP_{ND} variability across ROIs defined with MAN I was 2.6 ± 1.2% with the lowest BP_{ND} variability obtained in CD and the highest in SN (Fig. 6). The intra-operator BP_{ND} variability

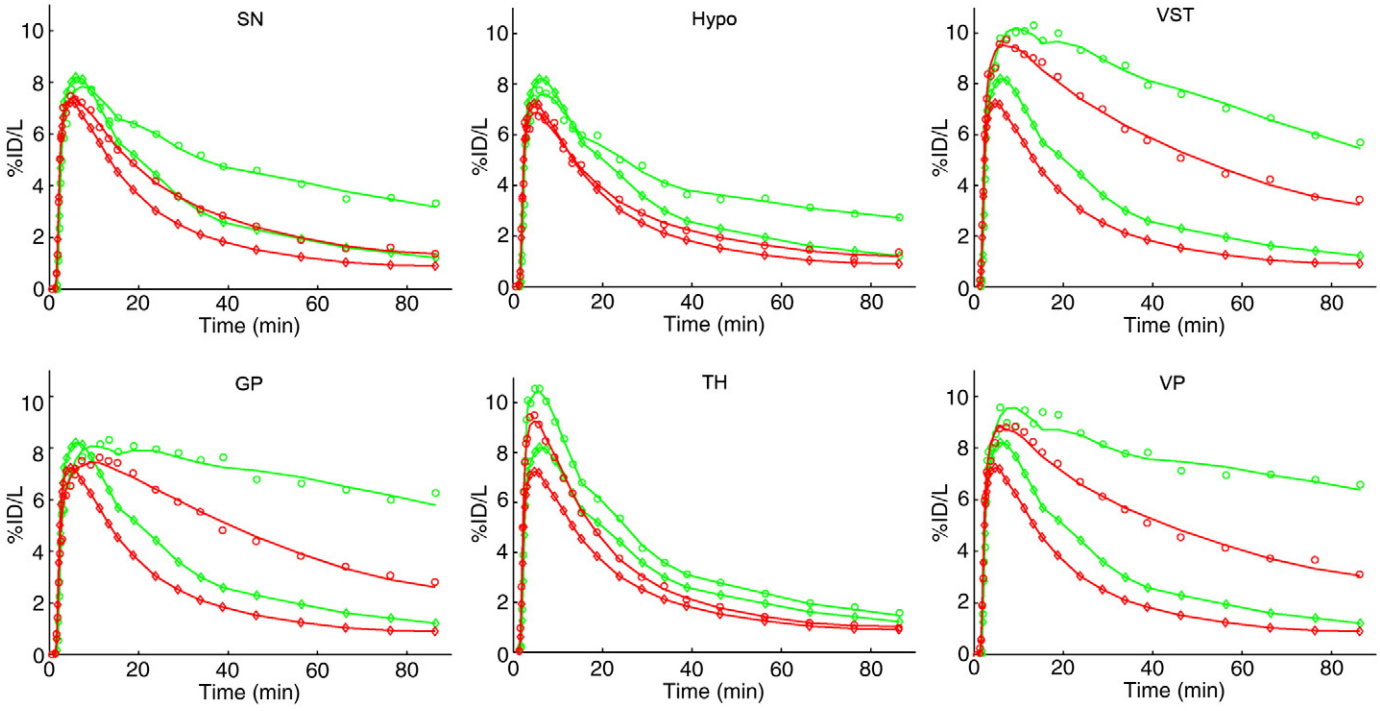

Fig. 3. [^{11}C] Time activity curves and SRTM model fits in a representative subject at baseline (—) and after oral administration of 175 mg of GSK598809 (—) showing: Hypo, SN, TH, VP_{SI}, VST and GP (○). On each plot, the TACs and model fits for Cerebellum (◊) at baseline (—) and after oral administration of 175 mg of GSK598809 (—) are plotted.

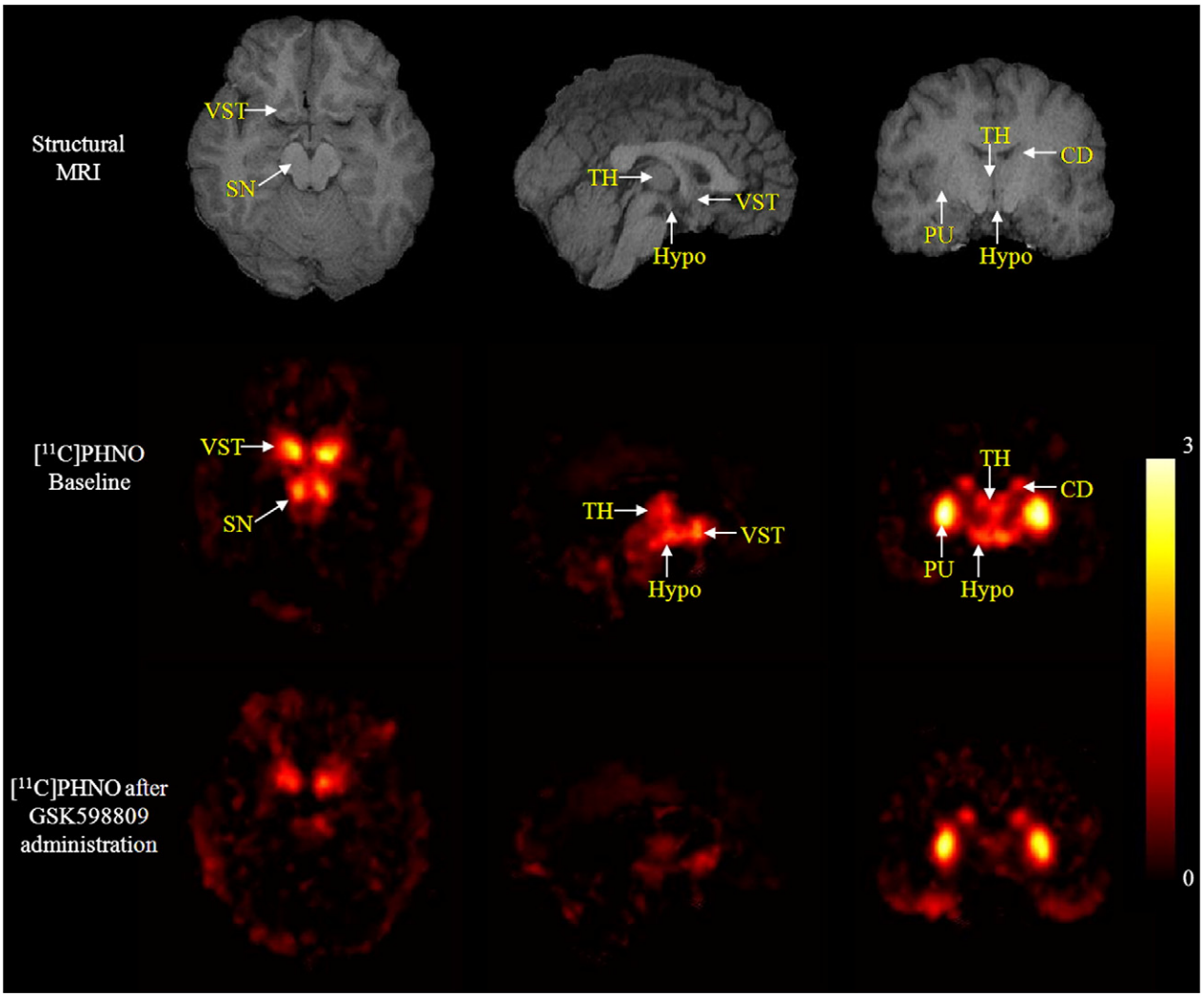

Fig. 4. [^{11}C]-(+)-PHNO BP_{ND} parametric image and MRI in one subject at baseline and after oral administration of 175 mg of GSK598809. A high BP_{ND} is observed in striatum, pallidum (GP and VP_{SI}), hypothalamus and substantia nigra and a lower inhomogeneous signal in thalamus. After the administration of GSK598809, a predominant reduction is observed in pallidum, Hypo and SN.

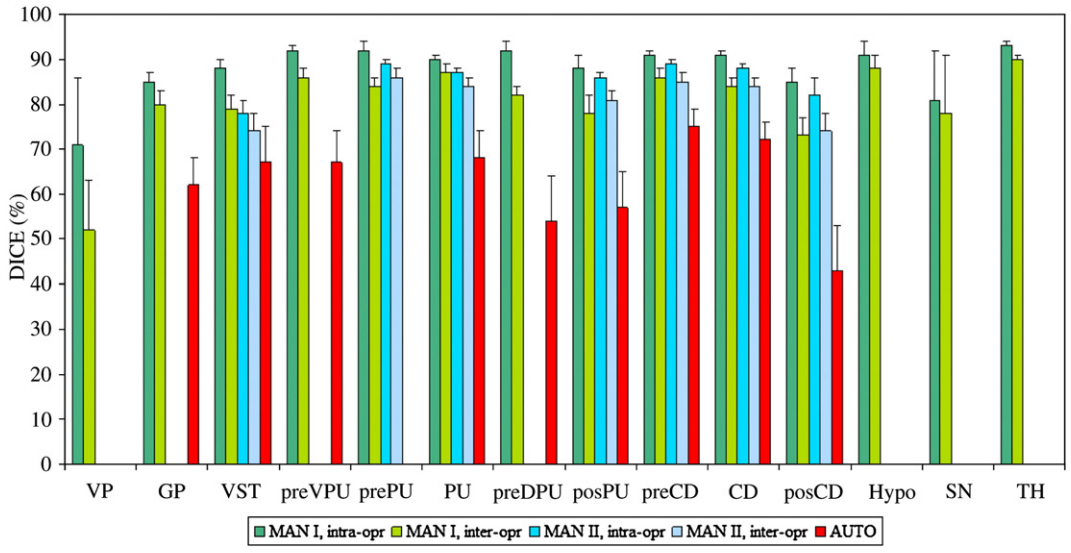

Fig. 5. DICE coefficient showing the ROI volume overlaps for methods: MAN I and MAN II (intra-/inter-operator) and the volume overlap between Automated and MAN I.

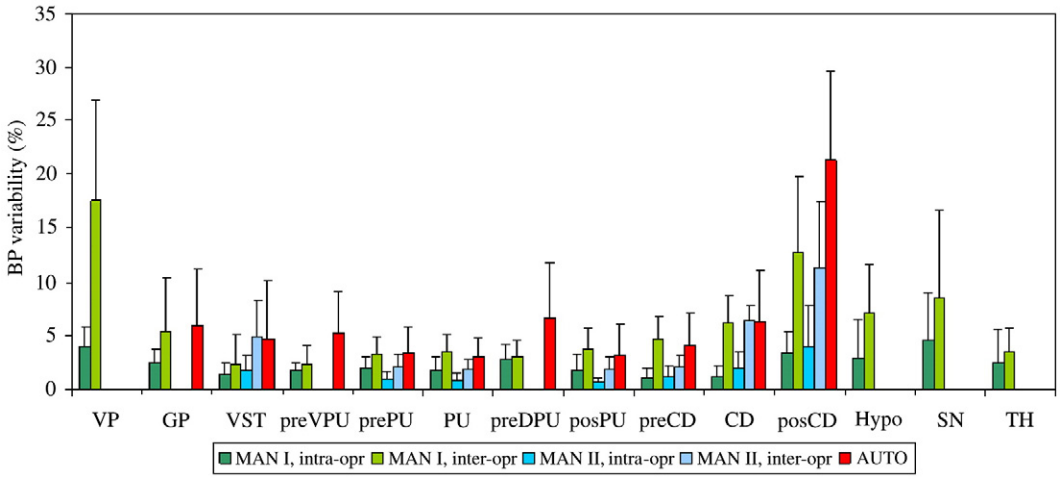

Fig. 6. [^{11}C]-(+)-PHNO BP_{ND} Variability for methods: MAN I and MAN II (intra-/inter-operator) and for Automated Vs MAN I.

for the striatal regions obtained with MAN I and MAN II, respectively, was 1.4 ± 1% and 1.7 ± 1.5% for VST, 1.7 ± 1.3% and 0.8 ± 0.7% for PU and 1.2 ± 1% and 2 ± 1.5% for CD. The average inter-operator BP_{ND} variability for MAN I across ROIs was 6.8 ± 4.8% with the lowest variability coming from VST and the highest from VP_{SI}. The inter-operator BP_{ND} variability for MAN I and MAN II for the striatal regions was VST: 2.3 ± 2.8% (MAN I) and 4.9 ± 3.4% (MAN II), PU: 3.5 ± 1.3% (MAN I) and 1.9 ± 0.9% (MAN II) and CD: 6.2 ± 2.7% (MAN I) and 6.4 ± 1.5% (MAN II). In Fig. 6, the BP_{ND} variability is displayed for all regions and methods. In addition to ROI volume overlap, the agreement between MAN I and MAN II was assessed by estimating the ICC for the BP_{ND} values obtained with the ROIs defined with the two methods and the values obtained are for VST ICC = 0.87, for CD ICC = 0.97 and for PU ICC = 0.91.

In this study, we also assessed the performance of an automated method that employed a non-linear warp of an anatomical atlas. To assess the method, we compared the automatically defined ROIs with the ROIs delineated manually with MAN I. The comparison between the automated method and manual (MAN I) gave an average DICE coefficient for the gross anatomical regions such as CD, PU, VST and GP of ~70 ± 4% (Fig. 5). For striatal subdivisions (preCD, posCD, posPU, preDPU and preVPU) the average DICE is ~65 ± 4%. The DICE for posCD and preDPU is lower and this might be due to the small size of these ROIs. To assess the relationship between volume overlap and ROI volume, the DICE coefficients for the manual (MAN I, intra- and inter-operator) and automated approaches were plotted against the ROI volume in Fig. 7. For ROI volumes not lower than 0.5 cm^3, DICE is relatively constant for the manual approach, although the DICE does drop off for GP. GP is a mixture of grey and white matter and this texture complicates delineation. DICE coefficients for the automated method also depend on the size of the ROI. Smaller regions yield lower DICE values, and this is consistent with mis-registration effects having bigger consequences for smaller regions.

The inter-method BP_{ND} variability was 4.9 ± 1.4% across all ROIs (excluding posCD which had high BP_{ND} variability). The inter-method DICE and BP_{ND} variability values for all regions are shown in Figs. 5 and 6, respectively.

D_3 receptor distribution

The D_3R anatomical distribution was investigated by using ROI driven regional and parametric analyses (methods A1, A2 and A3). The parameters of interest estimated for each ROI are the total [^{11}C]-(+)-PHNO BP_{ND}, the D_3R BP_{ND} (BP_{ND}^{D3}) and the associated fractional D_3R contribution (f_{PHNO}^{D3}). All regional estimates were derived with ROIs defined according to method MAN I and are shown in Table 3. Fig. 8 shows the parametric BP_{ND} and parametric f_{PHNO}^{D3} estimates (A2) plotted against estimates derived from regional TAC analyses (A1).

Figs. 9 and 10 show the total [^{11}C]-(+)-PHNO, the BP_{ND}^{D3} and BP_{ND}^{D2} at two brain locations with the corresponding ROIs overlaid. The two figures show that the majority of the signal from Hypo, SN, VP_{SI} and GP is due to D_3R. The BP_{ND}^{D3} in SN is not homogeneously distributed since a higher BP_{ND}^{D3} is observed in the rostral and medial parts of SN. A heterogeneous distribution is also observed in TH where a D_3R signal is seen in the rostral nuclei of the thalamus. In the striatum, on the other hand, the majority of the signal is due to the D_2R. In particular, in PU and dorsal CD the signal is entirely D_2R while in VST and ventral CD the signal is a mixture of D_2R and D_3R with the majority being D_2R. These visual observations are confirmed by the numerical estimates of f_{PHNO}^{D3} obtained from Eq. (1) as shown in Table 3. The estimated f_{PHNO}^{D3} values, in Hypo (~100%) and SN (~100%) indicate that the [^{11}C]-(+)-PHNO signal is predominantly attributable to the D_3R. In VP_{SI}, GP and TH this becomes less marked but the majority of the signal is still attributable to D_3R (VP_{SI} ≅ 70% and GP ≅ 60%, TH ≅ 60%). In VST the majority of the signal comes from the D_2R with D_3R only contributing ~20%. In the remaining regions, the [^{11}C]-(+)-PHNO signal is almost entirely due to D_2R with estimates of the D_3R component being very

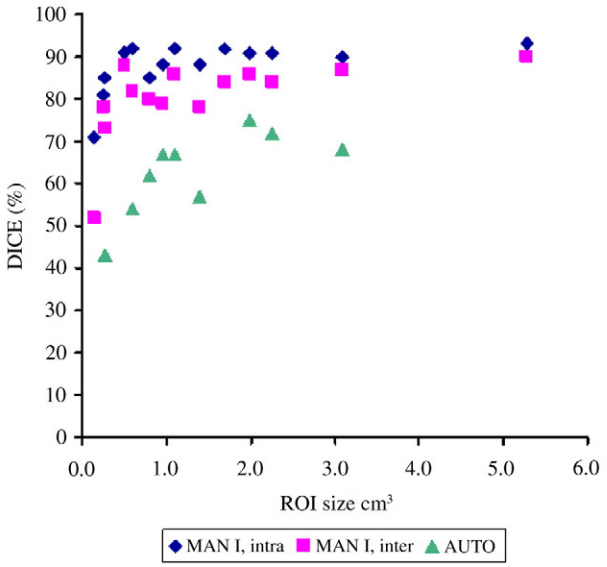

Fig. 7. DICE coefficient as a function of ROI size. Dice was obtained for the MAN I intra (♦)- and inter (■)-operator ROI volume overlap and for the Automated/MAN I ROI overlap (▲). The *x*-axis is the mean volume of each ROI estimated by MAN I (Table 1).

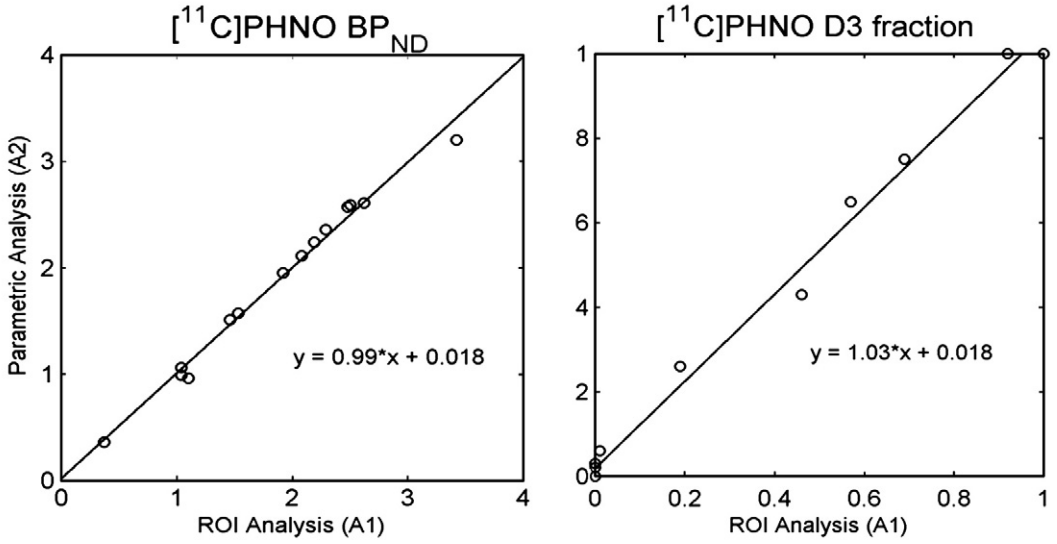

Fig. 8. Comparison of outcome measures of interest (BP_{ND} and f^{D3}_{PHNO}) derived from the ROI-based analyses (A1) and the parametric-based analyses (A2). Regression lines are close to the line of identity indicating a strong agreement between the two approaches for both parameters of interest.

small; for preVPU is 6%, while for preDPU, posPU, preCD and posCD is 0%. These distributions are in agreement with in vitro findings for D_3R (Murray et al., 1994; Gurevich and Joyce, 1999).

Discussions

We have developed robust guidelines (MAN I) for the delineation of the subcortical dopamine D_3R regions. Overall MAN I performed very well with high DICE coefficients and low BP_{ND} variability for both the intra- and inter-operator comparisons which demonstrates the high reproducibility of the method. The guidelines have been also tested on other T1_w settings and various image resolutions (0.78–1.5 mm) and achieve similar levels of reproducibility indicating the robustness of the method.

As mentioned above, several studies have shown that there is not a definitive anatomical, histological or histochemical distinction between the nucleus accumbens (NAC), CD and PU. Therefore, the VST guidelines presented in this manuscript and other published guidelines use various anatomical landmarks to define the dorsal boundary of the ventral striatum. The rationale for selecting Marker A and Marker B in these guidelines was based on the following: (a) the dorsal boundary encompasses the VST area as it is described in the literature. (b) The two regions (corpus callosum and CD) which are used to define the two landmarks are less variable, at least in healthy humans, compared to the landmarks used in other methods (i.e. ventricles, internal capsule, anterior commissure) and any potential variability does not seem to affect the definition and reliability of the VST ROI. These criteria have been applied on more than sixty subjects and on the average MNI template, and the defined VST ROI is well matched with the area described in the literature as VST based on its connectivity profile and (c) The definition of these markers is simple and reproducible and can be applied with high confidence even on low resolution data.

MAN I optimised the VST definition and the results indicate that MAN I outperformed MAN II for both DICE and BP_{ND} variability metrics. There is a 10% improvement in VST intra-operator DICE for MAN I over MAN II due to the more robust definition of the dorsal boundary of VST with MAN I. In particular, the definition of the dorsal boundary with MAN I involved connecting two predefined points which are placed before the tracing starts. MAN II is a more complex and subjective procedure as the operator needs to identify, on each slice, the most superior and lateral point of the internal capsule

Table 3
[11C]-(+)-PHNO Total, [11C]-(+)-PHNO D_3 BP_{ND} and [11C]-(+)-PHNO D_3 fractions with methods A1 and A2. Values in parentheses represent 95% confidence intervals. Method A1: ROIs were applied to the dynamic PET data; Method A2: ROIs were applied to the parametric images of BP_{ND}.

Region	Total [11C]-(+)-PHNO BPND		[11C]-(+)-PHNO D3 BPND		[11C]-(+)-PHNO D3 fraction	
	A1	A2	A1	A2	A1	A2
VP_{SI}	3.42 (3.30–0.54)	3.20 (3.08–3.31)	2.36	2.40	0.69 (0.59–0.79)	0.75 (0.59–0.91)
GP	2.62 (2.50–2.73)	2.61 (2.50–2.73)	1.49	1.70	0.57 (0.46–0.67)	0.65 (0.49–80)
Hypo	1.10 (0.98–1.21)	0.96 (0.85–1.08)	1.10	0.96	1 (0.78–1)	1 (0.68–1)
SN	1.04 (0.92–1.15)	0.99 (0.88–1.10)	0.96	0.99	0.92 (0.70–1)	1 (0.69–1)
TH	0.37 (0.26–0.49)	0.36 (0.25–0.47)	0.17	0.15	0.46 (0–1)	0.43 (0–1)
VST	2.48 (2.37–2.60)	2.57 (2.46–2.68)	0.47	0.67	0.19 (0.09–0.29)	0.26 (0.14–0.38)
PU[a]	2.19 (2.07–2.30)	2.24 (2.12–2.35)	0.00	0.00	0 (0–0.12)	0 (0–0.14)
preVPU	2.50 (2.39–2.62)	2.59 (2.48–2.70)	0.03	0.16	0.01 (0–0.12)	0.06 (0–0.18)
preDPU	1.92 (1.81–2.04)	1.95 (1.84–2.06)	0.00	0.00	0 (0- 0.14)	0 (0–0.16)
prePU[b]	2.29 (2.17–2.40)	2.36 (2.25–2.47)	0.00	0.07	0 (0- 0.11)	0.03 (0–0.16)
posPU	2.08 (1.96–2.19)	2.11 (1.99–2.22)	0.00	0.00	0 (0–0.13)	0 (0–0.15)
CD[c]	1.46 (1.35–1.58)	1.51 (1.39–1.62)	0.00	0.03	0 (0–0.18)	0.02 (0–0.23)
preCD	1.53 (1.41–1.64)	1.57 (1.46–1.68)	0.00	0.03	0 (0–0.17)	0.02 (0–0.22)
posCD	1.04 (0.93–1.16)	1.06 (0.95–1.18)	0.00	0.00	0 (0–0.25)	0 (0–0.30)

[a] prePU and posPU are combined.
[b] preDPU and preVPU are combined.
[c] preCD and posCD are combined.

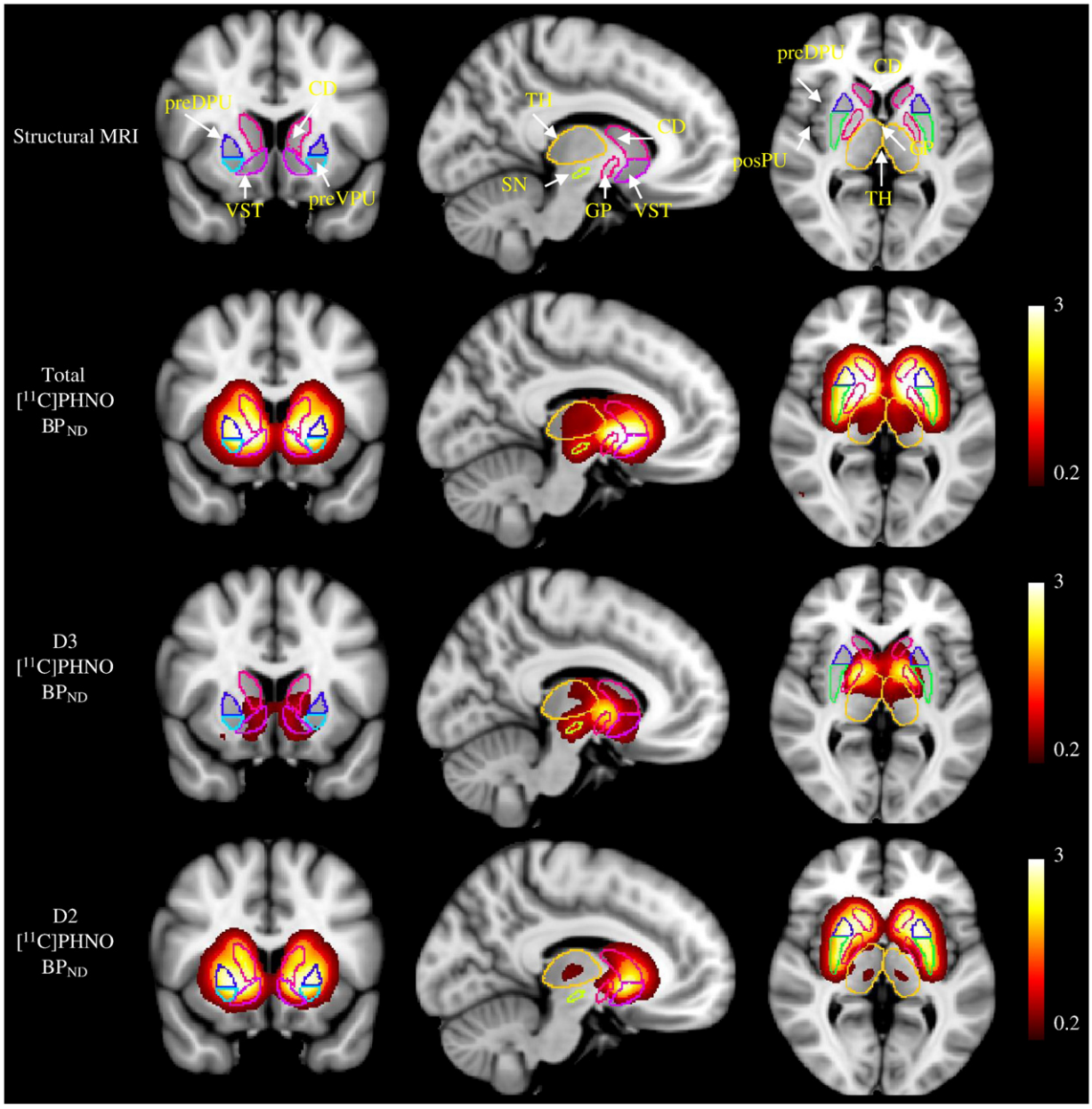

Fig. 9. Summary [^{11}C]-(+)-PHNO (Total, D_3 and D_2) BP_{ND} parametric images derived from all subjects in stereotaxic space overlaid onto the T1 weighted MNI template.

(sometimes difficult to identify) and the centre of the portion of the anterior commissure overlying the striatum. Another limiting factor about the VST definition with MAN II is that the anatomy of the area is such that sometimes the placement of the dorsal boundary with MAN II may not be optimal since it over-samples CD and/or PU.

The delineation of PU on the transverse plane with MAN I was faster than with MAN II (defined on coronal plane) and gives the operator better control over the ROI boundaries with GP and clastrum. However, the delineation of the ROI on the most ventral slices can be difficult and a good knowledge of the anatomy is required in order to sample the correct region. Therefore, following the delineation of PU on the transverse plane it is recommended that the operator switches to the coronal plane and optimises the intersection of PU and VST. It is important to note that the sub-parcellated striatal ROIs from MAN I (preVPU, preDPU, posPU, preCD, posCD) achieved similar DICE and BP_{ND} variability values to those of their gross anatomical regions i.e. CD and PU, indicating that MAN I is highly reproducible for smaller regions. Additionally, MAN I required less time for the ROI delineation and both operators mentioned that MAN I guidelines were applied with increased confidence in noisier images.

Overall, there was a good agreement between MAN I and MAN II which is reflected in the relatively high volume overlap between the ROIs defined with the two methods, the high ICC for the BP_{ND} values and the similarity of f^{D3}_{PHNO} estimates. In particular, Searle et al have estimated the f^{D3}_{PHNO} for MAN II using the same data set (Searle et al., 2010) and the values obtained are: VST, MAN I $-f^{D3}_{PHNO} = 26\%$ MAN II $-f^{D3}_{PHNO} = 26\%$, for CD MAN I $-f^{D3}_{PHNO} = 2\%$ MAN II $-f^{D3}_{PHNO} = 1\%$ and for PU MAN I $-f^{D3}_{PHNO} = 0\%$ MAN II $-f^{D3}_{PHNO} = 0\%$.

The performance of an automated method for the delineation of the aforementioned subcortical D_3R regions has been examined. Automated methods, such as the non-linear deformation of an anatomical atlas into the space of each individual, have the advantage of ease of examining large data sets at minimal time and completely

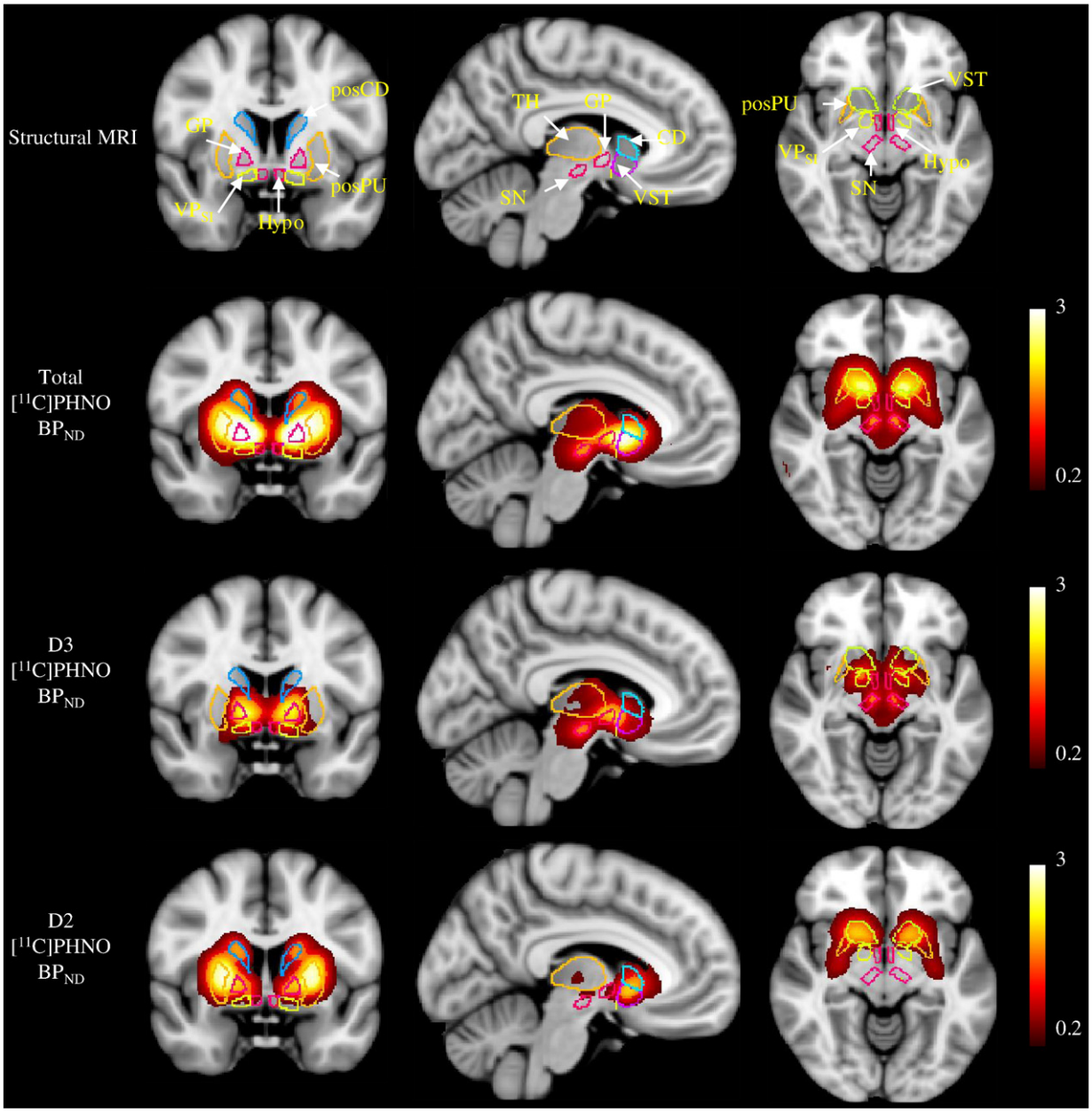

Fig. 10. Summary [^{11}C]-(+)-PHNO (Total, D_3 and D_2) BP_{ND} parametric images derived from all subjects in stereotaxic space overlaid onto the T1 weighted MNI template.

remove the *operator's subjectivity*. On the other hand, they are susceptible to misalignment, especially for small and subcortical structures, causing inevitable misclassifications. Here the agreement between AUTO and MAN I was moderate. As expected the inter-method DICE coefficient was not as high as with the MAN I intra-method values. However, the inter-method BP_{ND} variability is similar to the inter-operator variability across regions which indicates that the method could be used for estimation of BP_{ND} values in certain applications. Future work will investigate the application of more state-of-the-art non-linear registration algorithms that use improved mathematical algorithms and pay more attention to sub-cortical registration (Ashburner, 2007; Patenaude et al., 2007; Andersson et al., 2008).

In this study, we have identified and quantify the D_3R binding in two regions, the VP_{SI} and the Hypo, which had not been examined *in vivo* before even though there is *in vitro* evidence which supports the existence of D_3R. [^{11}C]-(+)-PHNO accumulation in Hypo was observed in the BP_{ND} parametric images (Figs. 4, 10). While we had some concern that the signal might be due to spillover effects from VP_{SI} and/or GP, the high f^{D3}_{PHNO} (~100%) and BP_{ND} values (1.17 ± 0.25) from both parametric and dynamic analyses along with the *in vitro* human (Staley and Mash, 1996; Gurevich and Joyce, 1999) and mice findings (Rabiner et al., 2009) suggest that the accumulation of [^{11}C]-(+)-PHNO here is due to the presence of D_3R in the Hypo. To our knowledge, this is the first examination of D_3R in the Hypo in human *in vivo*. Hypo receives input from the limbic regions and is implicated in a wide variety of neuropsychiatric disorders. Hypo is thought to be crucial for normal human behaviour and participates in a variety of autonomic and endocrine functions, sleep–wakefulness, appetite, emotions, etc. VP_{SI} has the highest [^{11}C]-(+)-PHNO BP_{ND} (BP_{ND} = 3.20) across regions and a high f^{D3}_{PHNO} (~75%). These results are in agreement with the *in vitro* studies (Murray et al., 1994; Gurevich and Joyce, 1999) that have identified ventral pallidum as a region with a high concentration of D_3R. We have to point out that the VP_{SI} includes

both ventral pallidum and the substantia innominata regions therefore a direct comparison with ventral pallidum data cannot be made. However, to examine how much of the ventral pallidum was included in the VP_{SI} ROI, the ROI was defined on a T1 image and overlaid on the co-registered T2-weighted image. Due to the high iron deposition in pallidum, the signal on a T2-weighted image is reduced making feasible the distinction of VP from the surroundings. We concluded that the ROI encompasses the VP very well and VP makes up the majority of its volume and for this reason in the ROI abbreviation the VP term was emphasised.

A high BP_{ND} signal was also observed in areas where the bed nucleus of stria terminalis (BNST) and extended amygdala are located (Fudge and Haber, 2001; Heimer, 2003). Extended amygdala has been accepted as a useful concept in investigation of drug addiction and neuropsychiatry disorders (Heimer, 2003) making this observation important, and increasing the need to investigate the existence of D_3R and D_2R in this region.

To assess the [^{11}C]-(+)-PHNO binding in striatum and to examine the D_3R in its functional subdivisions, we subdivided the striatum into precommissural/postcommissural CD, pre-commissural ventral and dorsal PU and postcommissural PU. The in vitro data suggest that there is a declining rostral to caudal gradient for the D_3R and also increased D_3R binding sites in the pre-commissural ventral PU. Statistical tests (paired t-tests) performed on the total [^{11}C]-(+)-PHNO BP_{ND} values between preDPU and preVPU and between preCD and posCD indicate that both pairs show a statistically significant difference for these subdivisions ($p<0.01$). Extraction of the D_3R BP_{ND} tends to verify these *in vitro* findings but the differences are marginal (Table 3).

Recent reports (Rabiner et al., 2009; Searle et al., 2010) have indicated a small dose-dependent decrease in cerebellum BP_{ND} following administration of selective D_3R antagonists (GSK598809 and SB-277011, respectively) which could lead to underestimation of the regional BP_{ND} values. The D_3R parametric BP_{ND} image showed a small signal in vermis (BP_{ND} ~0.25). We have examined occipital lobe, parietal lobe, frontal lobe, dorsal cerebellum and ventro-lateral cerebellum as potential reference regions. However, all of the candidate reference regions have a similar or equal signal decrease after the administration of GSK598809. Only the dorsal cerebellum shows a smaller decrease (regional BP_{ND} obtained with dorsal cerebellum are ~5% higher compare to regional BP_{ND} obtained with the whole cerebellum). However, the small size of this region contributes to poorer statistics; therefore, the whole cerebellum was selected as the most preferable choice for the reference region. Overall, considering the magnitude of these effects, there will be no significant impact on the dissection of the total [^{11}C]-(+)-PHNO BP_{ND} and the resultant BP_{ND}^{D3} and f_{PHNO}^{D3} estimates.

A limiting factor is that we cannot subdivide certain regions with the current MR and PET resolution. The *in vitro* findings suggest that in GP, TH and SN the D_3R are not homogeneously distributed. In particular the D_3R concentration in the internal GP, SN pars reticulata and anteroventral thalamic nucleus is higher. Furthermore, the D_3R distribution observed in these data (Fig. 9) suggests that there might be a different D_3R density in dorsal and ventral CD and an anterior–posterior heterogeneity in the GP distribution rather than internal–external heterogeneity. Therefore, a subdivision of these regions, based on functional data or anatomical data, should be considered. Advanced MR sequences, combined structural and functional data and/or increased PET resolution with cameras such as the HRRT (*Siemens* Medical Solutions, Knoxville, TN) may aid in the subdivision of these regions.

In this study, we have estimated the BP_{ND} and f_{PHNO}^{D3} with three approaches: A1, A2 and A3. Fig. 8 shows that there is an excellent agreement between the A1 and A2 approaches for both parameters of interest. For A3, the estimates are not quite as consistent, although this is expected since the non-linear registration applied here is not optimal for small subcortical structures and this consequently introduces errors into the estimates of BP_{ND} and f_{PHNO}^{D3}. This imperfect spatial normalisation is also reflected in the automated approach that gives low DICE and high BP_{ND} variability values. These mis-registration effects are more prominent in small anatomical regions (such as VP_{SI} and Hypo) as well as regions surrounded by a heterogeneous D_3R background such as VST, preVPU etc. Nevertheless, the A3 approach allowed us to visually investigate regions with moderate BP_{ND} but high f_{PHNO}^{D3}. Future studies, employing partial volume correction techniques (Aston et al., 2002; Shidahara et al., 2009) will be important to confirm whether signal in some of the smallest aforementioned regions is partially due to spillover effects.

In conclusion, using a selective D_3R antagonist and robust image analysis techniques it has been possible to dissect the regional D_3 signal from [^{11}C]-(+)-PHNO scans in humans *in vivo*.

Acknowledgments

The authors would like to acknowledge Charalampos Tsoumpas, Paul Shotbolt, Christopher Long, Qi Guo, and Vincent Cunningham for useful discussions and Robert Comley for his role in acquisition of the data.

References

Analyze. 1986. Rochester, Minneapolis, Biomedical Imaging Resource, Mayo Clinic.
Andersson, J., Smith, S., Jenkinson, M., 2008. FNIRT—FMRIB' non-linear image registration tool. Hum. Brain Map.
Ashburner, J., 2007. A fast diffeomorphic image registration algorithm. Neuroimage 38 (1), 95–113.
Aston, J.A.D., Cunningham, V.J., Asselin, M.C., Hammers, A., Evans, A.C., Gunn, R.N., 2002. Positron emission tomography partial volume correction: estimation and algorithms. J. Cereb. Blood Flow Metab. 22 (8), 1019–1034.
Cohen, M.X., Schoene-Bake, J.-C., Elger, C.E., Weber, B., 2009. Connectivity-based segregation of the human striatum predicts personality characteristics. Nat. Neurosci. 12 (1), 32–34.
Cumming, P., 2009. Imaging Dopamine. Cambridge University Press.
Defrise, M., Kinahan, P.E., Townsend, D.W., Michel, C., Sibomana, M., Newport, D.F., 1997. Exact and approximate rebinning algorithms for 3-D PET data. IEEE Trans. Med. Imaging 16 (2), 145–158.
Dice, L.R., 1945. Measures of the amount of ecologic association between species. Ecology 26 (3), 297–302.
Diedrichsen, J., 2006. A spatially unbiased atlas template of the human cerebellum. Neuroimage 33 (1), 127–138.
Duvernoy, H.M., 1999. The Human Brain: Surface, Blood Supply, and Three-Dimensional Sectional Anatomy. Springer-Verlag/Wien, New York.
Fudge, J.L., Haber, S.N., 2001. Bed nucleus of the stria terminalis and extended amygdala inputs to dopamine subpopulations in primates. Neuroscience 104 (3), 807–827.
Gallezot, J.-D., Beaver, J., Nabulsi, N., Weinzimmer, D., Slifstein, M., Gunn, R.N., Ding, Y.-S., Carson, R., Rabiner, E., 2009. ^{11}C]PHNO Studies in Rhesus Monkey: In vivo Affinity for D2 and D3 Receptors and Dosimetry. SNM, Toronto, Canada.
Gunn, R.N., Lammertsma, A.A., Hume, S.P., Cunningham, V.J., 1997. Parametric imaging of ligand-receptor binding in pet using a simplified reference region model. Neuroimage 6 (4), 279–2787.
Gurevich, E.V., Joyce, J.N., 1999. Distribution of Dopamine D3 receptor expressing neurons in the human forebrain comparison with D2 receptor expressing neurons. Neuropsychopharmacology 20 (1), 60–80.
Haber, S.N., Fudge, J.L., McFarland, N.R., 2000. Striatonigrostriatal pathways in primates form an ascending spiral from the shell to the dorsolateral striatum. J. Neurosci. 20 (6), 2369–2382.
Haber, S.N., Knutson, B., 2009. The reward circuit: linking primate anatomy and human imaging. Neuropsychopharmacology.
Haber, S.N., McFarland, N.R., 1999. The concept of the ventral striatum in nonhuman primates. Ann. NY Acad. Sci. 877 (1), 33–48.
Heimer, L., 2003. A new anatomical framework for neuropsychiatric disorders and drug abuse. Am. J. Psychiatry 160 (10), 1726–1739.
http://www2.bic.mni.mcgill.ca/.
Johansen-Berg, H., Behrens, T.E.J., Sillery, E., Ciccarelli, O., Thompson, A.J., Smith, S.M., Matthews, P.M., 2005. Functional-anatomical validation and individual variation of diffusion tractography-based segmentation of the human thalamus. Cereb. Cortex 15 (1), 31–39.
Lammertsma, A.A., Hume, S.P., 1996. Simplified reference tissue model for PET receptor studies. Neuroimage 4 (3), 153–158.
Martinez, D., Slifstein, M., Broft, A., Mawlawi, O., Hwang, D.-R., Huang, Y., Cooper, T., Kegeles, L., Zarahn, E., Abi-Dargham, A., Haber, S.N., Laruelle, M., 2003. Imaging human mesolimbic dopamine transmission with positron emission tomography. Part II: amphetamine-induced dopamine release in the functional subdivisions of the striatum. J. Cereb. Blood Flow Metab. 23 (3), 285–300.

Mawlawi, O., Martinez, D., Slifstein, M., Broft, A., Chatterjee, R., Hwang, D.-R., Huang, Y., Simpson, N., Ngo, K., Van Heertum, R., Laruelle, M., 2001. Imaging human mesolimbic dopamine transmission with positron emission tomography. I: accuracy and precision of D2 receptor parameter measurements in ventral striatum. J. Cereb. Blood Flow Metab. 21 (9), 1034–1057.

Murray, A.M., Ryoo, H.L., Gurevich, E., Joyce, J.N., 1994. Localization of dopamine D3 receptors to mesolimbic and D2 receptors to mesostriatal regions of human forebrain. Proc. Natl. Acad. Sci. U. S. A. 91, 11271–11275.

Narendran, R., Slifstein, M., Guillin, O., Hwang, Y., Hwang, D.-R., Scher, E., Reeder, S., Rabiner, E., Laruelle, M., 2006. Dopamine (D2/3) receptor agonist positron emission tomography radiotracer [^{11}C]-(+)-PHNO is a D3 receptor preferring agonist in vivo. Synapse 60 (7), 485–495.

Parent, A., Hazrati, L.-N., 1995. Functional anatomy of the basal ganglia. I. The cortico-basal ganglia-thalamo-cortical loop. Brain Res. Rev. 20 (1), 91–127.

Patenaude, B., Smith, S., Kennedy, D., Jenkinson, M., 2007. FIRST—FMRIB's integrated registration and segmentation tool. Human Brain Mapping Conference.

Rabiner, E.A., Slifstein, M., Nobrega, J., Plisson, C., Huiban, M., Raymond, R., Diwan, M., Wilson, A.A., McCormick, P., Gentile, G., Gunn, R.N., Laruelle, M., 2009. In vivo quantification of regional dopamine-D3 receptor binding potential of (+)-PHNO: Studies in non-human primates and transgenic mice. Synapse 63 (9), 782–793.

Searle, G., Beaver, J., Comley, R.A., Bani, M, Tziortzi, A., Slifstein, M., Mugnaini, M., Wilson, A.A, Merlo-Pich, E., Houle, E., Gunn, R.N, Rabiner, E, Laruelle, M., 2010. Imaging dopamine D_3 receptors in the human brain with positron emission tomography, [^{11}C]PHNO, and a selective D_3 receptor antagonist. Biological Psychiatry. 68 (4), 392–399.

Shidahara, M., Tsoumpas, C., Hammers, A., Boussion, N., Visvikis, D., Suhara, T., Kanno, I., Turkheimer, F.E., 2009. Functional and structural synergy for resolution recovery and partial volume correction in brain PET. Neuroimage 44 (2), 340–348.

Smith, S.M., 2002. Fast robust automated brain extraction. Hum. Brain Mapp. 17 (3), 143–155.

Sokoloff, P., Giros, B., Martres, M.-P., Bouthenet, M.-L., Schwartz, J.-C., 1990. Molecular cloning and characterization of a novel dopamine receptor (D3) as a target for neuroleptics. Nature 347, 146–151.

Staley, J.K., Mash, D.C., 1996. Adaptive Increase in D3 Dopamine Receptors in the Brain Reward Circuits of Human Cocaine Fatalities. J. Neurosci. 16 (19), 6100–6106.

Wellcome Trust Centre for Neuroimaging "http://www.fil.ion.ucl.ac.uk/spm".

Willeit, M., Ginovart, N., Kapur, S., Houle, S., Hussey, D., Seeman, P., Wilson, A.A., 2006. High-affinity states of human brain dopamine D2/3 receptors imaged by the agonist [^{11}C]-(+)-PHNO. Biol. Psychiatry 59 (5), 389–394.

Wilson, A.A., McCormick, P., Kapur, S., Willeit, M., Garcia, A., Hussey, D., Houle, S., Seeman, P., Ginovart, N., 2005. Radiosynthesis and evaluation of [^{11}C]-(+)-4-Propyl-3, 4, 4a, 5, 6, 10b-hexahydro-2H-naphtho[1, 2-b][1, 4]oxazin-9-ol as a potential radiotracer for in vivo imaging of the dopamine D2 high-affinity state with positron emission tomography. J. Med. Chem. 48 (12), 4153–4160.